The Influence of Bathymetry Over Heat Transport Onto the Amundsen Sea Continental Shelf

Michael Haigh[1] [ID], **Paul R. Holland[1]** [ID], and **Adrian Jenkins[2]** [ID]

[1]British Antarctic Survey, Cambridge, UK, [2]Department of Geography and Environmental Sciences, Northumbria University, Newcastle upon Tyne, UK

Abstract Ice streams such as Pine Island and Thwaites Glaciers which terminate at their ice shelves in the eastern Amundsen Sea, West Antarctica, are losing mass faster than most others about the continent. The mass loss is due to basal melting, which is influenced by a deep current that transports warm Circumpolar Deep Water (CDW) from the continental shelf break toward the ice shelves. This current and associated heat transport are controlled by factors such as bottom bathymetry, near-surface winds and meltwater. Using a realistic regional model as a reference, in this study we use idealized models to examine the role of bathymetric features in determining the shelf-wide circulation and in enabling heat transport from the deep ocean onto the continental shelf. We find that a ridge that blocks deep westward inflow from the Bellingshausen Sea enables a deep cyclonic circulation on the shelf with an eastward undercurrent immediately south of the shelf break. Inclusion of the ridge enhances heat transport onto the continental shelf; without the ridge the flow features an along-shelf break westward current that suppresses cross-shelf break fluxes. We also consider the effects of shifting the prescribed wind forcing profile to the south—a simplified representation of future potential changes to the winds—and we find that the continental shelf is warmer in this scenario. These fundamental investigations will help refine the aims of future fieldwork and modeling.

Plain Language Summary The ice streams that drain into the Amundsen Sea, West Antarctica, are losing mass faster than most others about the continent. Relatively warm ocean waters have access to the undersides of these ice shelves, and are thought to be the cause of the great mass loss. Deep currents transport warm waters from the deep ocean in the north toward the Antarctic coast in the south, but the details of such currents are not certain. Complex regional models which simulate the physics in the Amundsen Sea region have been useful examining the involved physical processes. In this study we use a sequence of simpler models to develop a more fundamental understanding of these processes. In particular, these simple models allow us to thoroughly investigate the role that ocean floor bathymetry plays in determining the flows in the region. We find that a ridge that blocks deep inflow from the east enables a clockwise circulation on the continental shelf, without which transport of heat onto the continental shelf would be greatly reduced. This result improves our understanding of the present flow and heat transport in the Amundsen Sea, and will aid predictions of the future of the region.

1. Introduction

The ice streams that drain into the Amundsen Sea, West Antarctica, are losing mass faster than most others about the continent (Rignot et al., 2008; Shepherd et al., 2018). In particular, Pine Island Glacier and Thwaites Glacier are major mass sinks for the West Antarctic Ice Sheet (Joughin et al., 2014; Mouginot et al., 2014; Rignot et al., 2014). The ice sheets are losing mass as a result of rapid basal melting of the ice shelves that extend over and float on the ocean's surface (Jourdain et al., 2022; Pritchard et al., 2012). This basal melting is due to the access that warm Circumpolar Deep Water (CDW), which is ~3°C above the local freezing point, has to the bases of the floating ice shelves (Dutrieux et al., 2014; Heywood et al., 2016; Jacobs et al., 1996; Walker et al., 2007). Concerns for the region are intensified due to the bottom topography at the grounding lines of the ice shelves that deepens shoreward, a configuration associated with the potential marine ice sheet instability (Favier et al., 2014; Joughin et al., 2014).

In the Amundsen Sea, two major controls of the flow and the access of CDW to the ice shelves in the region are the winds and bottom bathymetry. In Figure 1a we show the Bedmachine bathymetry (Morlighem, 2020) and the ERA-5 surface stresses (more details in Section 2.1) as used in this study in a reference regional model. Figure 1b

**Writing – review & editing:** Paul R. Holland, Adrian Jenkins

shows the bathymetry in the eastern Amundsen Sea embayment in finer detail, with four bathymetric features of interest highlighted. These are the Pine Island-Thwaites West/East (PITW/PITE) troughs, the central basin (C) and a ridge (R) to the east of the PITE trough. In this study, by using models with idealized representations of these bathymetric features we elucidate their role in shaping the shelf-wide circulation on and heat transport onto the continental shelf. Our main finding is that the ridge is vital for enabling the cyclonic circulation in the eastern Amundsen Sea and for facilitating transport of CDW onto the continental shelf.

In many sections around Antarctica, warm and salty CDW is excluded from the continental shelf by the Antarctic Slope Front (ASF) at the continental slope. The ASF separates the CDW from fresher, cooler waters above and to the south (Ou, 2007; Stewart et al., 2019; Stewart & Thompson, 2013) and is maintained (at least partially) by coastal easterlies that drive downwelling at the Antarctic coast that pushes down isopycnals (Jacobs, 1991; Jacobs et al., 2012; Jenkins et al., 2016; Thompson et al., 2018). A compensating sea-surface height gradient of opposite sign at the surface means that the ASF is commonly associated with a westward surface current which weakens with depth, transitioning to an absolute eastward undercurrent near the ocean bottom. While there are observations (Walker et al., 2007, 2013) and model diagnoses (Caillet et al., 2022; Dotto et al., 2019; Kimura et al., 2017; Thoma et al., 2008; Webber et al., 2019) of an ASF at the Amundsen Sea continental slope, this is weaker than in most other regions around Antarctica (Thompson et al., 2018). A variety of mechanisms can contribute to the weaker ASF in the Amundsen Sea, including the weak and variable surface wind patterns (Raphael et al., 2016), frequent cross-shelf eddy intrusions (Klinck & Dinniman, 2010) and the lack of dense shelf water formation in the region (Petty et al., 2013; Thompson et al., 2018). With a weaker ASF, CDW floods the continental shelf in the Amundsen Sea, and therefore has great access to the ice shelves, contributing to the large melt rates in the region.

An undercurrent flowing eastward along the continental shelf break is thought to be important for heat transport onto the continental shelf. Walker et al. (2013) observed this undercurrent flowing upstream of the PITW trough. Guided by geostrophic f/h (Coriolis frequency/water column depth) contours, this current turns southward when it encounters the PITW trough, as observed by Assmann et al. (2013) and Walker et al. (2007, 2013), transporting warm CDW across the shelf break in the process. The fate of this deep current or its consistency is not certain given the spatially and temporally limited extent of the data. Numerical model results (Dotto et al., 2020; Kimura et al., 2017; Nakayama et al., 2018; Thoma et al., 2008; Webber et al., 2019) suggest this warm current turns back to the east after entering the PITW trough and makes a second southward turn at the PITE trough before continuing toward the ice shelves.

The undercurrent and the thickness of the on-shelf CDW layer are highly variable across a range of timescales. In particular, decadal variability in the undercurrent and CDW layer thickness, which are linked to variability in the wind forcing (Dutrieux et al., 2014; Kimura et al., 2017; Thoma et al., 2008), leads to decadal variability in basal melting (Jenkins et al., 2018). Holland et al. (2019) suggest that a climatic westerly trend in the shelf break winds has led to periods of stronger eastward flow in recent decades, potentially enhancing the transport of warm CDW toward the ice shelves and accelerating melting. Ice-ocean simulations presented by Naughten et al. (2022) add evidence to the notion that warming and accelerated melting in the Amundsen Sea over the last century are driven by anthropogenic changes to the shelf break winds and the associated effects on the eastward undercurrent (see their Figure 2). However, more recent work by Holland et al. (2022) found that significant trends are limited to the deep ocean, where the westerlies have been intensifying due to anthropogenic effects (Arblaster & Meehl, 2006; Gillett et al., 2013; Goyal et al., 2021).

Given the cyclonic winds, the basin-wide flow in the eastern Amundsen Sea is predominantly cyclonic, both at the surface and at depth. Regional models (Caillet et al., 2022; Donat-Magnin et al., 2017; Jourdain et al., 2017, 2019; Kimura et al., 2017; Thoma et al., 2008; Webber et al., 2019) are well-suited for studying this flow, but interpreting their outputs can be difficult due to the large number of interacting processes that act across many timescales. In addition, these models include complex bathymetries with which it is difficult to discern the role of specific bathymetric features in shaping the shelf-wide flow. In this study we progressively develop an idealized model of the eastern Amundsen Sea to improve our understanding of the present-day shelf-wide dynamics as captured in a companion regional model. Our main aim is to elucidate the role of bottom bathymetry in shaping the circulation and in facilitating heat transport toward the ice shelves. We will also consider the effects of a southward shift of the zonal winds. The intention is that the conclusions of this study will allow for more confident predictions of the fate of the Amundsen Sea and its ice shelves. It is also anticipated that the results of this study will help to refine the aims of future fieldwork and modeling investigations.
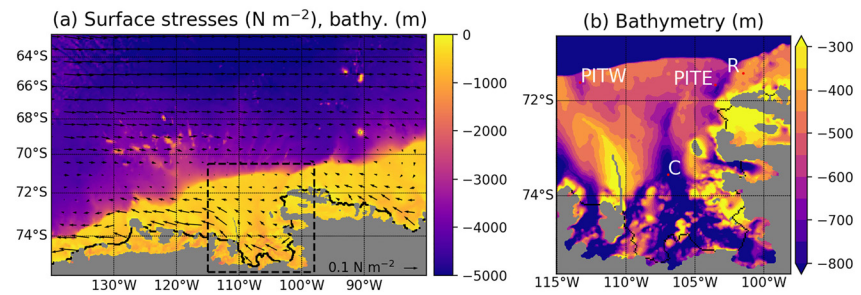
Figure 1. (a) Time-mean (1979–2011) surface stress (arrows) accounting for sea ice, used to force the reference regional model. Color represents the bottom bathymetry (units m). The dashed box outlines the eastern Amundsen Sea, in which we will focus our attention. Gray masking represents land and the solid black contour represents the edge of the floating ice shelves at the ocean surface. (b) Bottom bathymetry in the eastern Amundsen Sea region (units m). Four bathymetric features are highlighted: the Pine Island-Thwaites West (PITW) trough, the deep central basin (C), the Pine Island-Thwaites East (PITE) trough and the ridge (R).

This study is organized as follows. In Section 2 we describe the output from a realistic regional model of the Amundsen Sea. This will represent a benchmark to which idealized model results can be compared. In Section 3.1 we introduce the idealized model and describe the wind, temperature and salinity forcing regimes. Through Section 3.2 we progressively update the bathymetry to reproduce important bathymetric features, and we discuss their influence in the resulting flow responses. In Section 3.3 we discuss the heat transport across the shelf break in these simulations. Next, in Section 3.4 we consider the effects of a southward shift of the zonal winds. Lastly, in Section 4 we summarize and discuss our results.

## 2. Regional Model

2.1. Model Details

For the regional model we use checkpoint 65s of the Massachusetts Institute of Technology general circulation model (MITgcm) in a configuration similar to that of Bett et al. (2020) and Kimura et al. (2017). This is also the same model and configuration used by Naughten et al. (2022), with one minor difference in the fixed iceberg flux field. The model domain extends from 140°W to 80°W and from 75.5°S to 62°S. The lateral grid resolution is 0.1° in longitude, such that the isotropic grid step is ~2.75 km in the south of the domain and ~5.15 km in the north. The vertical direction is discretized by 50 levels with the thinnest (10 m) levels near the surface and the thickest (200 m) levels near the ocean bottom.

Lateral viscosity is represented using the Leith scheme in the horizontal and a constant Laplacian viscosity is used in the vertical. Vertical diffusion of potential temperature θ and salinity S is parameterized using the K-profile parameterization scheme (Large et al., 1994), while there is no explicit lateral diffusion of θ and S. Ice shelves and sea ice provide interactive sources and sinks of freshwater. A free-slip condition is applied at the lateral boundaries and quadratic bottom friction is applied at the ocean floor.

The model is forced by six-hourly ERA5 10 m winds, precipitation, surface long-wave and short-wave radiation, 2 m air temperature and specific humidity, and atmospheric pressure. Open boundary conditions in the west, north and east are derived from the World Ocean Atlas for salinity and potential temperature. For the ocean velocities and sea ice properties the boundary conditions are derived from the Southern Ocean State Estimate (Mazloff et al., 2010). The model is spun up using the 1979–2002 interval of the external forcing data. After this spinup, forcing is restarted from 1979, the beginning of the analysis period of the regional model. All data that we present are obtained by averaging outputs between January 1979 and December 2011.

Figure 1a shows the time-mean surface stress with sea ice accounted for. Also shown is the Bedmachine (Morlighem, 2020) bottom bathymetry and the outline of the eastern Amundsen Sea region in which we focus our attention. Surface stresses are typically eastward to the north of the continental slope and westward to the south of the continental slope. Along the continental slope the surface stress is close to zero, but the stress curl is strongly cyclonic, corresponding to upwelling velocities.

Figure 1b shows the bottom bathymetry in the eastern Amundsen Sea. Labeled are four bathymetric features that we identify as being particularly important for the oceanography of the eastern Amundsen Sea. These
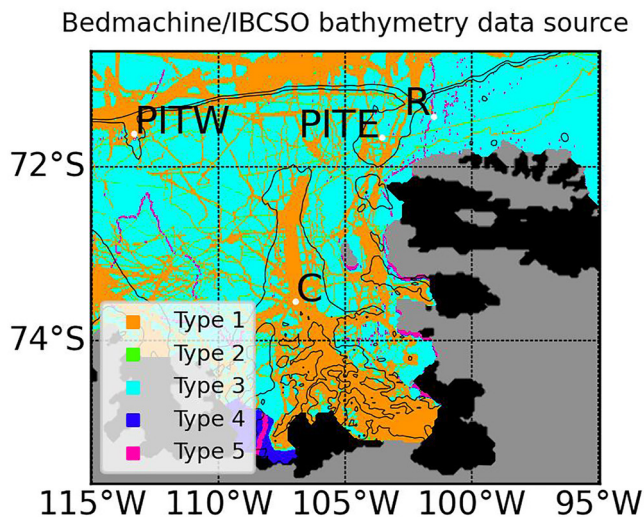
Figure 2. Data source types for the Bedmachine/IBCSO bottom bathymetry in the eastern Amundsen Sea from Dorschel et al. (2022b). Type 1: Depth value collected by a multibeam echo-sounder. Type 2: Combination of direct measurement methods. Type 3: Interpolated based on a computer algorithm. Type 4: Depth value is an interpolated value guided by helicopter/flight-derived gravity data. Type 5: Depth value is taken from a pre-generated grid that is based on mixed source data types, for example, single beam, multibeam, interpolation etc. This is a subset of all possible data source types; see Dorschel et al. (2022b) for further details. Gray masking represents the Antarctic continent and black masking represents ice shelves.

are the PITW trough, the central basin (C), the PITE trough and the ridge (R). Many studies have discussed the importance of the troughs and basin (usually also referred to as a trough), but not the ridge. In the Bedmachine (Morlighem, 2020) topography the ridge is of approximately 400 m depth and lies to the west of similarly shallow topographic features between the Amundsen and Bellingshausen Seas. While the ridge blocks deep inflow from the east, some deep inflow is also blocked upstream in the Bellingshausen Sea.

The Bedmachine bottom bathymetry is derived from the IBCSO v2 dataset (Dorschel et al., 2022b), in which the data are derived from direct measurement methods or algorithms where direct measurements are lacking. Figure 2 summarizes the data source types in the eastern Amundsen Sea; see the figure caption for descriptions of each data source type. While much of the eastern Amundsen Sea has been mapped via multibeam echo-sounding, in the on-shelf region between the Amundsen and Bellingshausen Seas there are few direct observations. This includes the ridge, the data for which are predominantly determined via interpolation algorithms. As such, the true properties of the ridge are uncertain, but it is nonetheless present in regional simulations of the Amundsen Sea. Its role in shaping the circulation in these simulations and the real Amundsen Sea is little discussed.

2.2. Model Output

Figure 3a shows the time-mean (1979–2011) near-surface (depth $z = -5$ m) flow and potential temperature in the eastern Amundsen Sea, as outputted by the regional model (Bett et al., 2020; Kimura et al., 2017; Naughten et al., 2022). Near the surface, a cold fresh current enters the eastern Amundsen Sea from the Bellingshausen Sea via the narrow shelf region bounded to the south by the coast and to the north by the continental shelf break. The current then turns southward and cyclonically traverses the eastern Amundsen Sea before exiting in the west toward the Dotson Ice Shelf. Surface stratification (vertical gradient in salinity) makes it possible for the surface flow to pass over the deep central basin, rather than be blocked by it. The primary reason for the surface current following the coast is the southward Ekman transport caused by the westward surface stresses that create a shoreward sea surface height (SSH) gradient along the coast. This surface current is often referred to as the Antarctic Coastal Current (AACC) (Moffat et al., 2008; Schubert et al., 2021). Another current is the Antarctic Slope Current (ASC) (Chavanne et al., 2010; Dong et al., 2016) which is locked to the continental slope, but is thought to have a weak signal in the real Amundsen Sea (Thompson et al., 2020), as is the case in the regional model output.
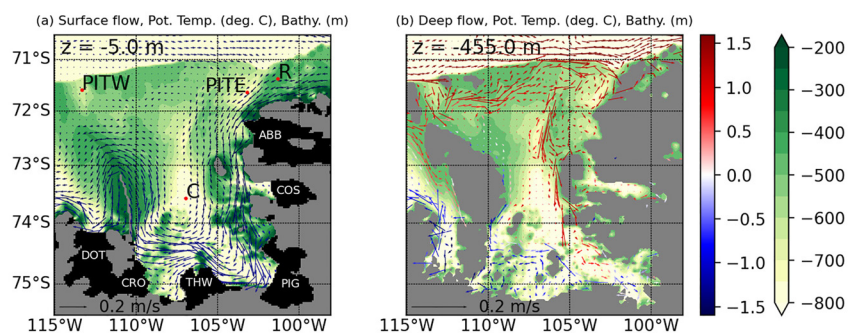
Figure 3. (a) The surface (depth $z = -5$ m) time-mean flow (arrows) and potential temperature (arrow color, °C) in the eastern Amundsen Sea. (b) The deep ($z = -455$ m) time-mean flow and potential temperature in the eastern Amundsen Sea. In both panels, the background color depicts the bottom bathymetry and gray masking represents land. In panel (a) black masking represents the ice shelves. Labeled are the Dotson, Crosson, Thwaites, Pine Island Glacier, Cosgrove and Abbot ice shelves.
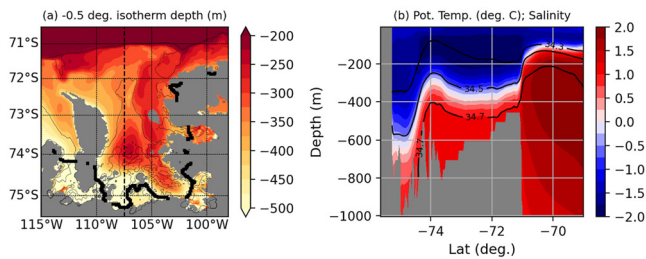
Figure 4. (a) The time-mean $-0.5°C$ isotherm depth (m). Gray areas represent land or locations where the isotherm doesn't exist. The thin black contours represent the $-1,000$ and -600 m bathymetric contours. The thick black contour represents the fronts of the ice shelves. (b) A latitude-depth slice of the time-mean potential temperature at 107.5°W, the longitude depicted by the dashed line in (a). The black lines are the 34.3, 34.5 and 34.7 g/kg salinity contours.

Figure 3b shows the time-mean deep ($z = -455$ m) flow and potential temperature. The deep flow consists of a warm current that circulates the eastern Amundsen Sea cyclonically. Since the ridge blocks deep inflow from the east, waters for this flow are predominantly sourced from an eastward undercurrent that originates west of 115°W, travels along the continental slope and turns onto the shelf via the PITW trough. This flow is similar to the observations of Assmann et al. (2013) and Walker et al. (2013). A similar process occurs at the PITE trough. The PITW trough is connected to the PITE trough by east-west oriented geostrophic f/h contours (between 71°S and 72°S), along which the current travels after entering the PITW trough. Once reaching the PITE trough (near 105°W), the current is blocked by the f/h contours of the trough and turns southward; the current does not travel into the trough, but rather along its flank. The current then passes by the eastern side of the central basin, toward the ice shelves.

As the deep current circulates by the coast and the floating ice shelves it entrains cold fresh meltwater and becomes more buoyant. This causes the current to shoal and permits it to move above bottom topography that is shallower than the upstream southward-flowing current ($z = -455$ m for the level shown). The outflowing deep current (not visible in Figure 3b) then follows roughly the same bathymetric contours (Bear Ridge) as the near-surface current, which guide it out of the eastern Amundsen Sea.

The Amundsen Sea flow is highly variable over a range of timescales. As an example, at some instances in time both the deep and depth-integrated flows in the eastern Amundsen Sea feature a closed cyclonic circulation, but this is not strong enough to have a signal in the time mean. Our focus is on the mean circulation with the intention that this will aid future investigations into deviations from this mean.

Figure 4a shows the time-mean $\theta = -0.5°C$ isotherm depth in the eastern Amundsen Sea. This illustrates the access that warm CDW has to the continental shelf, and is very similar to the model results of Webber et al. (2019). The isotherm is relatively shallow to the east of the central basin, with a warm tongue extending from the shelf break to the ice shelves. Comparing with Figure 3b, the role of the deep flow in transporting heat southwards from the shelf break is clear. However, the mechanisms that transport CDW southwards across the shelf break are less clear. Figure 3b implies that simple onshore advection by the mean current through the PITW trough is one possible mechanism. The connectedness of the shallow $\theta = -0.5°C$ isotherm from the shelf break via the PITE trough to the south suggests the PITE trough is also important for cross-shelf break heat transport. Cross-shelf break heat transport at the PITE trough and elsewhere along the continental shelf can be due to processes such as mean advection, eddy advection, flow in bottom Ekman layers and/or transient wind-driven intrusions (Klinck & Dinniman, 2010).

The location of the ASF is illustrated in Figure 4a by the southward deepening of the isotherm along the continental slope (near 71°S). The latitude-depth slice of the time-mean potential temperature θ at 107.5°W in Figure 4b shows the ASF in finer detail. The salinity (S) contours plotted in Figure 4b confirm the ASF is a front in all three of potential temperature, salinity and density. In many sections around Antarctica the ASF intersects the continental shelf or slope (Thompson et al., 2018), but in the Amundsen Sea the ASF is weaker and CDW floods the lower section of the on-shelf water column.

3. Idealized Model

3.1. Model Details

For the idealized model we use the same MITgcm 65s checkpoint, but in a greatly simplified configuration. The domain is a zonally periodic channel of side length 600 km in the zonal direction and 500 km in the meridional direction. We use an f-plane domain with reference Coriolis parameter $f_0 = -1.4 \times 10^{-4}$ s^{-1}, corresponding to a reference latitude of 74.27°S. The domain is discretized onto a uniform $N_x \times N_y = 240 \times 200$ grid, corresponding to a lateral grid resolution of 2.5 km. This lateral resolution may not be large enough to resolve all mesoscale eddies on the continental shelf (Stewart & Thompson, 2015), but we do not expect a finer resolution to affect the conclusions of this study. The vertical direction is discretized by 50 levels each 20 m thick. As in the regional
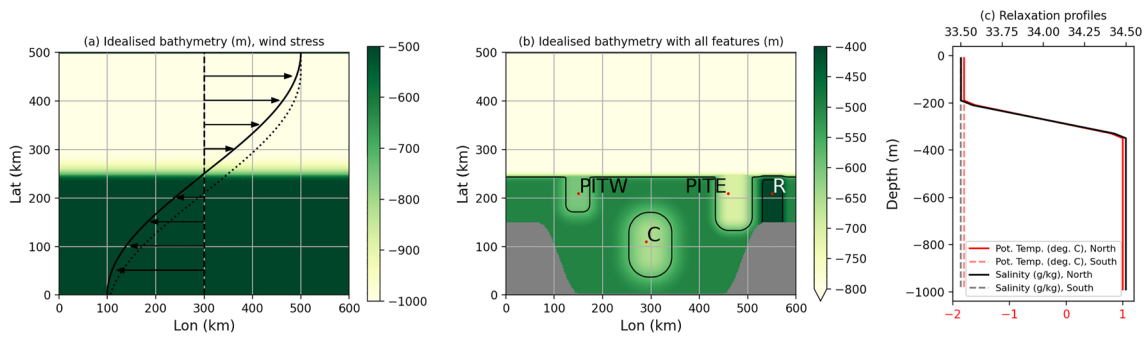
Figure 5. (a) The continental shelf bottom bathymetry used in the idealized model (color). The solid curve and arrows represent the steady, zonally uniform wind stress profile which has a maximum absolute stress of 0.025 N m⁻² attained at the northern and southern boundaries. The dashed line represents zero wind stress. The dotted curve is the original wind stress profile translated south by 40 km, used in Section 3.4. (b) Bathymetry for the idealized model with reproductions of the four bathymetric features of interest. Gray masking represents land. (c) The relaxation profiles versus depth for potential temperature (red, °C) and salinity (black, g/kg). Solid lines represent the profiles for the northern boundary and dashed lines are for the southern boundary.

model, free-slip boundary conditions are applied at the walls and quadratic bottom friction is applied at the ocean floor.

We use a continental shelf domain, with shallower (500 m depth) waters in the south and deeper (1,000 m depth) waters in the north, as shown in Figure 5a. Off-shelf, the real Amundsen Sea is much deeper, but the weak communication between off-shelf deep waters and on-shelf waters means modeling the very deep off-shelf flow is not necessary. Also shown in Figure 5a is the steady, zonally uniform cosine-shaped zonal wind stress. The wind stress is eastward in the north, with a maximum stress of 0.025 N m⁻² at the northern boundary, and westward in the south, with a minimum stress of −0.025 N m⁻² at the southern boundary. The wind stress at the center of the continental slope is zero, at which point the wind stress curl (which is cyclonic everywhere) is maximized. This wind stress profile and magnitude are intended to reproduce the surface stress curl and upwelling/downwelling velocities associated with the mean surface stresses in the regional model (Figure 1a). In Section 3.4 we consider the effects of a southward shift of the wind profile, motivated by predicted changes to the winds in the Amundsen Sea region.

Figure 5b shows the bathymetry for the idealized model with representations of all four features of interest: PITW (600 m depth) trough, PITE (700 m depth) trough, the central basin (C, 650 m depth) and the ridge (R, 400 m depth). Walls on the continental shelf outline the idealized eastern Amundsen Sea basin. Different combinations of the bathymetric features will be used in idealized model simulations, starting from the zonally uniform setup in Figure 5a. Precise details of the bathymetry that we do not account for in the idealized model will lead to differences in the details of the flow responses in the idealized and regional models. However, our focus is on the larger-scale qualities of the flow and heat transport.

Each simulation is globally initialized with zero flow, potential temperature $\theta = -1.8°C$ and salinity $S = 33.5$ g/kg. These choices for θ and S represent cold and fresh initial conditions. Potential temperature θ and salinity S are forced by a relaxation with a 10-day timescale at the northern boundary to the profiles shown in Figure 5c (solid lines). These profiles are motivated by observations in the region (Arneborg et al., 2012; Assmann et al., 2013; Dutrieux et al., 2014; Walker et al., 2007, 2013) and output from the regional model. The prescribed pycnocline is between 200 and 340 m depth, throughout which the temperature and salinity both increase linearly with depth. This pycnocline separates cold fresh ($\Theta = -1.8°C$, $S = 33.5$ g/kg) surface waters from warm salty ($\theta = 1°C$, $S = 34.5$ g/kg) CDW at depth.

The relaxation in the north is the only source of CDW for the idealized model. Therefore, by forcing the model in this way and by using the cold fresh initial conditions we guarantee that the only source for on-shelf CDW is southward advection across the continental shelf break. This is useful given our aim to study the role of winds and bathymetry in controlling access of CDW to the continental shelf in the eastern Amundsen Sea.

At the southern boundary θ and S are relaxed with a timescale of 100 days back to their cold and fresh initial conditions, an idealized representation of freshwater fluxes due to ice shelf melt. This additional weak buoyancy forcing is necessary to maintain a realistic on-shelf heat distribution in steady state; without this the continental
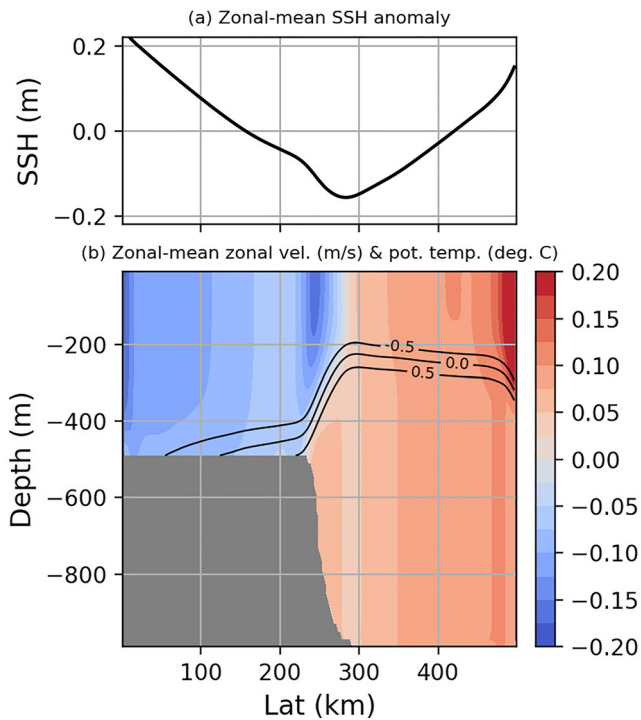
Figure 6. Outputs from the zonally uniform idealized model. (a) Zonal-mean sea surface height (SSH) anomaly (vs. latitude) averaged over the final year of a 30-year simulation. (b) Time-mean, zonal-mean zonal velocity (units m s^{-1}) versus latitude and depth. Positive (red) corresponds to eastward flow and negative (blue) corresponds to westward flow. In (b) the black lines represent the −0.5, 0 and 0.5°C contours of θ, with colder contours nearer the surface. These isotherms are also a proxy for salinity and density.

shelf in the idealized model becomes too warm. Simulations without relaxation in the south (Figure S1 in Supporting Information S1) confirm this to be true, but the flow fields in these simulations are qualitatively similar to the flow fields in the simulations with the southern relaxation. That the weak southern relaxation is required to achieve a realistic on-shelf heat distribution highlights the importance of ice shelf melt or other freshwater fluxes to the thermodynamic balance in the real world and regional model. The relaxations imposed at the southern and northern boundaries are tapered to zero over a range of four grid points inward from the boundary.

The model includes vertical (10^{-3} m^2 s^{-1}) and horizontal (10 m^2 s^{-1}) viscosity and weak biharmonic diffusion (non-dimensional grid-dependent biharmonic viscosity of 0.1) to ensure model stability. Potential temperature and salinity are subject to vertical diffusion (10^{-5} m^2 s^{-1}) but no horizontal diffusion. Because of the linearity of the advection-diffusion equation and the linear equivalence of the θ/S initial conditions and relaxation profiles, θ and S are mathematically equivalent. This means that the salinity and density distributions at any time in the simulation can be inferred from the temperature distribution and vice-versa. The simulation outputs that we show are after 30 years of model runtime, sufficient for the flow, temperature and salinity fields to have reached equilibrium.

3.2. Flow Responses

3.2.1. Zonally Uniform Case

We first present model output for the zonally uniform case. In this case all results are approximately zonally uniform on lengthscales larger than the mesoscale eddy scale. Figure 6a shows the zonal-mean SSH anomaly averaged over the final year of a 30-year simulation. The V-shaped SSH profile is the consequence of southward wind-driven Ekman transport in the south and northward transport in the north, which creates a convergence of mass at the southern and northern boundaries.

Figure 6b shows the zonal-mean, time-mean zonal velocity (color) and potential temperature (contours). The difference between the warm northern and cold southern relaxations creates a net-southward deepening of the isotherms. This southward deepening is also contributed to by Ekman downwelling at the southern boundary that pushes down on-shelf isopycnals and forces CDW off the shelf (Jacobs, 1991; Jenkins et al., 2016). The northward gradient in potential temperature—which exists also in salinity and density, for which potential temperature is a proxy—becomes concentrated at the continental slope, forming an ASF.

The ASF forms because baroclinic instability is suppressed over the continental slope due to the large contribution to the meridional potential vorticity (PV) gradient q_y by the rapidly changing bottom bathymetry (C. Chen & Kamenkovich, 2013; S.-N. Chen et al., 2020) (baroclinic instability requires a change in the sign of q_y in the vertical direction [Vallis, 2017]). This effect reduces excitation of baroclinic eddies over the continental slope, but not over flat-bottomed areas of the ocean. Therefore, while baroclinic eddies act to flatten the isotherms and isopycnals over the flat-bottomed areas of the ocean, this effect is suppressed over the continental slope so the sharp ASF persists. At times the ASF can be sufficiently steep such that the PV gradient associated with the lateral density gradient is large enough to cancel with the contribution from the bottom slope. At such instances baroclinic eddies can be generated, leading to a weakening of the ASF, and restoration of stability. See Figure S2 in Supporting Information S1 where we consider the PV gradient.

The flow (Figure 6b) is eastward in the north and westward in the south, and is strongly barotropic away from the continental slope. Although the ASF causes the flow at the continental slope to be more eastward with depth (via the thermal wind relation), this effect is only strong enough to produce a weak eastward flow on the upper section of the continental slope and does not lead to a strong eastward undercurrent along the shelf break. This is in contrast to the regional model that has strong eastward flow along much of the shelf break, as visible in Figure 3b.
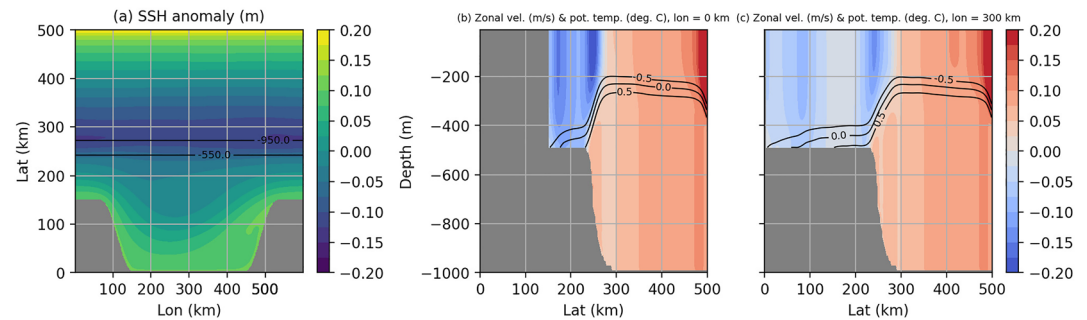
Figure 7. Outputs averaged over the final year of a 30-year simulation of the idealized model with a walled bay region on the shelf. (a) A plan view of the sea surface height (SSH) anomaly (units m). Also plotted are the −950 and −550 m contours of the bottom bathymetry. (b) A latitude-depth slice of the zonal velocity (units m s^{-1}) at a "walled" longitude, $x = 0$ km. (c) A latitude-depth slice of the zonal velocity (units m s^{-1}) at a "bay" longitude, $x = 300$ km. In panels (b) and (c) the black lines are the −0.5, 0 and 0.5°C contours of θ. The potential temperature contours are also exact contours of salinity and density.

Above the ASF there is a fast westward current, consistent with the strong southward SSH gradient at the same latitudes. That this westward current exists above the ASF could be interpreted as the reason for the weak eastward undercurrent. However, it is more accurate to say the weak eastward undercurrent relative to the regional model is due to the zonal symmetry and periodicity of the idealized model. In such a model, there is a lack of mechanisms for meridional transfer of zonal momentum, which means that any zonal momentum imparted at the surface by the wind stress must be removed at the ocean bottom via bottom friction at the same latitude. Therefore, the zonal flow near the ocean floor is dictated by the winds, as it must generate the bottom friction that opposes the wind stress. This is not an exact balance because the model includes lateral viscosity and the flow features non-zero time-mean meridional overturning Ekman flow. However, the weakness of the viscosity and the Ekman flow means they make negligible contributions to the zonal-mean zonal momentum budget. We conclude that the westward surface current must exist to compensate for the ASF: without the strong westward surface current, the deep eastward flow would be too strong and too much eastward momentum would be removed by bottom friction at these latitudes.

A consequence of the deep flow being approximately set by the surface stress is that changes in the θ and S relaxation (e.g., adjusting the pycnocline height) will change the SSH gradient and surface flow in the balanced flow response, but cannot notably change the deep flow. For example, shifting the pycnocline downwards in the relaxation profiles will reduce the net height change in the ASF at the continental slope, which means that above the ASF the southward SSH gradient and westward surface current must weaken in order for the same velocities to be realized at the ocean floor (thus providing the bottom stress required to balance the surface stress).

3.2.2. Adding Walls to the Continental Shelf

We now add walls to the continental shelf to create an area similar to the eastern Amundsen Sea (Figure 7). The off-shelf dynamics do not change in any notable way since this part of the domain is not changed. On-shelf the inclusion of walls leads to the zonal blockage of a large range of f/h contours, meaning that velocity and vorticity balances cannot be attained in the same way as in the case without walls.

In Figure 7a we show the SSH anomaly in the updated domain, averaged over the final year of the 30-year simulation. Figure 7b shows the zonal velocity u at a "walled" longitude, $x = 0$ km and Figure 7c shows u at a "bay" longitude, $x = 300$ km. As in the zonally uniform case, the flow is strongly barotropic at most locations. At the walled longitudes (Figure 7b) the wind-driven southward mass convergence at the coast maintains a SSH gradient with a relatively small latitudinal range of shelf over which baroclinic eddies can act to flatten the gradient. The result is a relatively fast barotropically unstable (the meridional PV gradient changes sign in the meridional direction [Vallis, 2017]) westward coastal current. After entering the bay the current broadens (Figure 7c), as characterized by a less steep SSH gradient.

Figures 7b and 7c show that the flow response features a second westward current that is attached to the continental slope, in addition to the coastal current. At the walled longitudes, the two currents run close to one another, while they have a broad separation at the bay longitudes. The two westward currents in this configuration of the idealized model can be interpreted as simple representations of the AACC and the ASC. While the AACC is
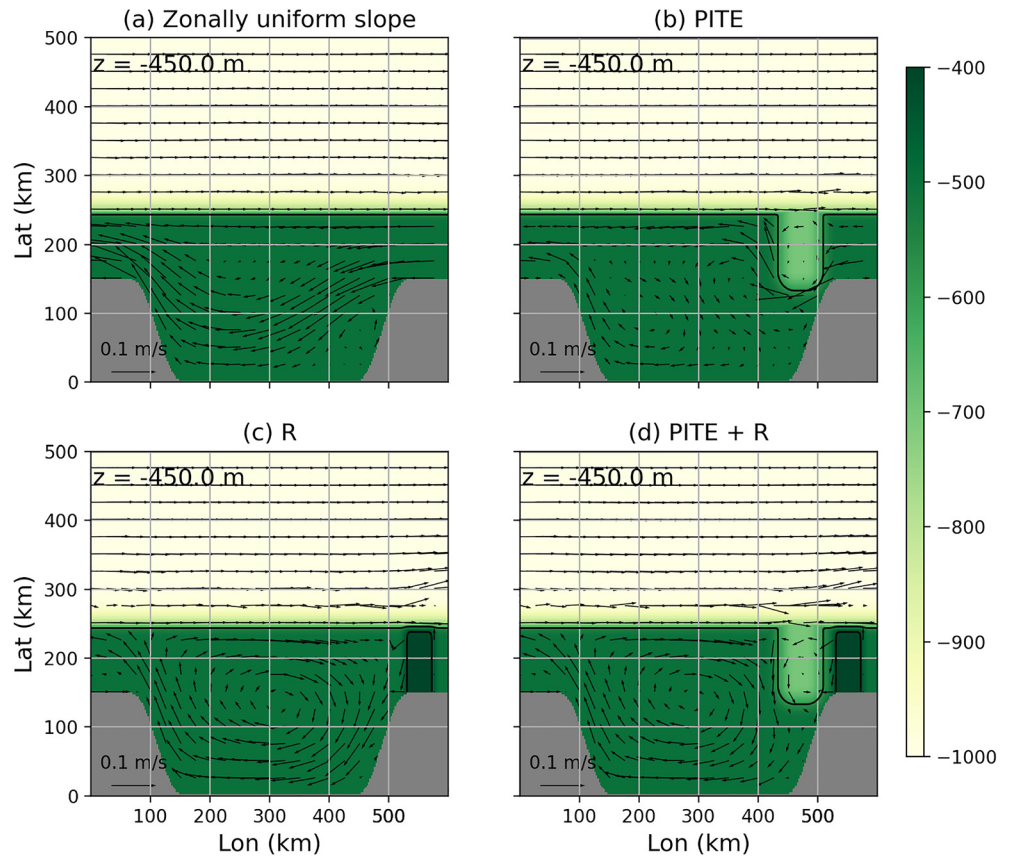
Figure 8. Vector plots of the deep flow ($z = -450$ m) averaged over the final year of 30-year simulations for a selection of bottom bathymetries in the idealized model. (a) Deep flow in the case of no bathymetric features, that is, the same simulation as in Figure 7. (b) Deep flow with a trough in the east. (c) Deep flow with a ridge in the east. (d) Deep flow with the Pine Island-Thwaites East (PITE) trough and ridge. In all panels color represents the bottom bathymetry and the black contours are the -580 and -420 m isobaths.

present in the regional model and the real world, the ASC is not present in the regional model and is thought to have a weak signal in the real Amundsen Sea (Thompson et al., 2020). The ASC has too strong a signal in this idealized model, in effect due to the ASF beneath; at these latitudes where the domain is zonally uniform and periodic, the strong SSH gradient and associated ASC are required in order to compensate for the ASF, so that the weak surface stresses can be balanced by weak bottom friction in the zonal momentum budget.

3.2.3. Adding the PITE Trough and Ridge

We now add the PITE trough and ridge to the bathymetry of the idealized model. Figure 8 shows the deep flow ($z = -450$ m) for a selection of bottom bathymetries. For reference, Figure 8a shows the deep flow for the case of no bottom bathymetry on the shelf, the same simulation as in Figure 7. In the simulation with just the PITE trough (Figure 8b), the deep westward flow (and surface flow, not shown) is made up of two currents, one which remains attached to the shelf break after passing to the south of the PITE trough and one which meanders in its wake. The overall result is a flow pattern that is not topologically distinct from the simulation with a zonally uniform slope (Figure 8a).

In the case with just a ridge (Figure 8c) we observe a qualitatively different flow compared to cases without a ridge. Deep inflow from the east is now blocked by the ridge, just as in the regional model. Since there is now blocking of PV contours in the zonal direction at all latitudes on the shelf, vorticity balance cannot be maintained by a periodic flow, unlike in the zonally uniform case. Instead, vorticity imparted at the surface by the cyclonic winds is extracted at the ocean floor by a deep cyclonic circulation and the associated bottom friction. This also means that unlike in the zonally uniform case, the (approximately) locally balanced zonal momentum budget does not exist. In short, by adding a ridge to the continental shelf the on-shelf dynamics have switched from
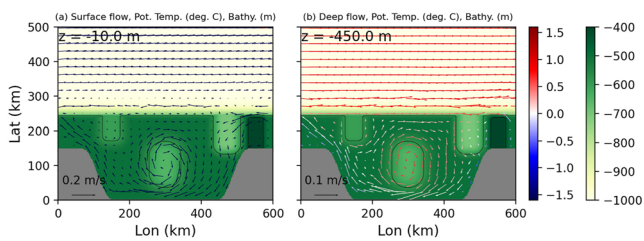
Figure 9. The flow response in the idealized model with the Pine Island-Thwaites West trough, central basin, Pine Island-Thwaites East trough and ridge. Shown are (a) the surface ($z = -10$ m) flow and (b) the deep ($z = -450$ m) flow. In both panels arrow color represents the local potential temperature, background color represents the bottom bathymetry and the black contours represent the -580 and -420 m isobaths. All data are averaged over the final year of a 30-year simulation.

being analogous to those of the Antarctic Circumpolar Current to those of a North Atlantic Gyre. In particular, the addition of the ridge induces an eastward undercurrent immediately south of the shelf break—this latter feature is absent in simulations without a ridge. This undercurrent is part of the broader cyclonic circulation and turns southwards when it encounters the ridge in the east.

If the ridge were inverted to be a trough with f/h contours that intersect with the boundary, then we would attain a flow response similar to the case with just the PITE trough (see Figure S3 in Supporting Information S1). In this case, despite there being no periodic f/h contours on the shelf, deep flow still passes over this inverted ridge. This is because in our parameter regime the topographic form stresses associated with flow across the bathymetric contours of the trough can be balanced by nonlinear advection of westward momentum across the trough. Such a balance is achieved with westward flow that accelerates as it starts to cross the trough and decelerates as it approaches the flat section of bathymetry on the other side.

Compared to the case with just the ridge, inclusion of both the PITE trough and ridge (Figure 8d) leads to a cyclonic circulation which is shifted slightly to the west. This is because the PITE trough blocks the eastward current from traveling any further to the east and directs it instead to the south, as in the regional model. Also as in the regional model, we emphasize that the undercurrent does not flow in the depths of the PITE trough.

To summarize, these results suggest that by blocking deep inflow from the east, the ridge enables a deep cyclonic flow that spans the eastern Amundsen Sea embayment. This circulation includes an eastward undercurrent flowing along the northernmost section of the continental shelf and along the shelf break. Without the ridge, deep inflow from the east would counter this undercurrent. This finding sheds light on why in the real Amundsen Sea the eastward undercurrent which originates upstream of the PITW trough can turn on shelf and flow eastward along the northern section of the shelf break. In this section we have not shown the surface flow. For the PITE case, the surface flow is similar to the zonally uniform case shown in Figure 7. For cases with a ridge, the surface flow no longer has an ASC flowing westward above the continental slope, meaning in these cases the surface flow is closer to the reference regional simulations shown in Figure 3. We show this effect of the ridge on the surface flow in the next section.

3.2.4. Adding the Central Basin and PITW Trough

We now add a central basin and PITW trough to the idealized bathymetry. Figure 9 shows the surface (a, $z = -10$ m) and deep (b, $z = -450$ m) flow and potential temperature in the resulting simulation. The surface flow (Figure 9a) features a cold and fresh coastal current which enters the domain from the east, passes to the south of the central basin and leaves the domain in the west. The inclusion of ridge eliminates the westward-flowing ASC over the continental slope, leading to a flow field closer to that of the regional model (Figure 3a). The surface current is similar in the simulations without the central basin (not shown), the main difference being the central basin causing the current to cross the bay further to the south. When it enters the bay from the east, the mean surface flow tends to pass to the north of the ridge, rather than directly over it. If we included near-surface stratification (in salinity) in the idealized model, as is present in the regional model, this would permit the surface current to pass directly over the ridge, as it does in the regional model (Figure 3a). The surface flow features a notable cyclonic circulation, in particular in the central basin, which is stronger than in the regional model due to the abundance of closed f/h contours in the idealized bathymetry.

At depth (Figure 9b) the main feature of the flow is the cyclonic circulation. As before, the northern limb of this circulation is the eastward undercurrent which turns south when it becomes blocked by the PITE trough. Like in the regional model (Figure 3b), this southward flow proceeds from the western edge of the PITE trough to the eastern edge of the central basin. To the east of the central basin is where the deep flow is warmest, due to the southward advection of warm waters that have recently broken across the shelf—we discuss this heat transport more in the next section.

The undercurrent continues on a cyclonic trajectory about the central basin. After passing to the south and west of the central basin, the majority of this flow leaves the bay to the west. The remainder of the flow remains in the bay

and forms a closed cyclonic circulation about the central basin. A closed deep circulation such as in this idealized model is commonly observed at specific instances in time in the regional model, but is not consistent enough to have a marked signal in the mean flow (Figure 3b). Most of the deep flow that has left the bay to the west in the idealized model is forced to turn and reenter the bay to the west of the PITW trough. The small remainder continues flowing west and passes to the north of the ridge; this latter flow feature is not present in the regional model.

The PITW trough plays a smaller role in the idealized model compared to the regional model. In both models an eastward current flowing along the continental slope and shelf break turns into the PITW trough. This current overshoots the western rim of the trough and crosses f/h contours in a manner similar to the simulations of Assmann et al. (2013). While in the regional model these waters tend to remain on the shelf—aided by f/h contours between the PITW trough and the central basin—this is less common in the idealized model given its simpler bathymetry. Instead, in the idealized model there is only a weak mean flow of waters that escape the confines of the PITW trough (mainly near its south-eastern corner) to reach the flat sections of the shelf.

3.3. Heat Transport

3.3.1. Heat Fluxes

In this section we discuss the transport of heat onto the continental shelf and the role of bathymetric features in the idealized model. We first consider the area-integrated cross-shelf heat fluxes (through the latitude $y = 240$ km). We define the heat flux as $\rho_0 C_p v(\theta - \theta_0)$, where v is the meridional velocity, $\rho_0 = 1,030$ kg m^{-3} is the reference density and $C_p = 3,974.0$ J kg^{-1} C^{-1} is the heat capacity. For the reference temperature we use $\theta_0 = -1.8°C$, the value used for the uniform initial condition. The local freezing temperature could have been used instead, from which we would make the same conclusions.

In Figure 10 we show time series of the monthly area-integrated cross-shelf heat fluxes. In each case we show the total cross-shelf heat flux, the heat flux across longitudes where the shelf topography is zonally uniform, and the heat flux across longitudes where there is a trough or ridge. All total cross-shelf heat fluxes are negative (southwards) and can be so in equilibrium because of the cooling by the relaxation at the southern boundary. The time series are largely insensitive to adjustments of a few grid points to the limits of the longitudinal sections.

Figure 10a shows cross-shelf heat fluxes for the bathymetry with just the PITE trough. In this case the heat fluxes at the PITE trough and the uniform longitudes are strongly anti-correlated, with the two time series summing to a small negative value. This behavior is due to an along-shelf break westward current that meanders when it encounters the trough. The net on-shelf heat flux is balanced by heat removal by the relaxation at the southern boundary. This net transfer of heat onto the shelf is only marginally greater than in the uniform shelf case (see next section for evidence of this).

Figure 10b shows cross-shelf heat fluxes for the bathymetry with the PITE trough and ridge. This simulation has net heat fluxes across the shelf break approximately twice as large as the simulation with just the PITE trough (Figure 10a), illustrating the role of the ridge in enhancing cross-shelf break heat transport. Almost all of this heat is fluxed onto the shelf at the longitudes of the PITE trough and ridge, and most of the heat fluxed onto the shelf is fluxed off the shelf at uniform longitudes. Figure 10c shows cross-shelf break heat fluxes for the bathymetry with the two troughs, the ridge and the central basin. Results are similar to those in the PITE trough and ridge case (Figure 10b), the main difference being the additional source of heat provided by fluxes at the PITW trough. This additional on-shelf heat flux is compensated for by greater off-shelf heat fluxes at the uniform longitudes. The result is a net on-shelf heat flux approximately the same as in the PITE trough and ridge case.

These time series illustrate the role that along-shelf topographic variability plays in enhancing cross-shelf break heat fluxes. In the case of a zonally uniform shelf break, the only physical processes by which heat can be fluxed onto the shelf are baroclinic instability and bottom Ekman transport. The latter is negligibly small in our simulations and the former mechanism is suppressed by the bottom gradient associated with the continental slope.

By adding troughs and/or a ridge to the uniform shelf break additional mechanisms can now induce southward flow and heat fluxes across the shelf break. Small-scale topographic variability at the troughs/ridges on the shelf break causes breaks in geostrophy and induces southward flow across the shelf break. Figure S4 in Supporting Information S1 compares the lateral momentum terms with the corresponding pressure gradient forces to illustrate that deviations from geostrophic balance occur over the topographic features. Small-scale topographic
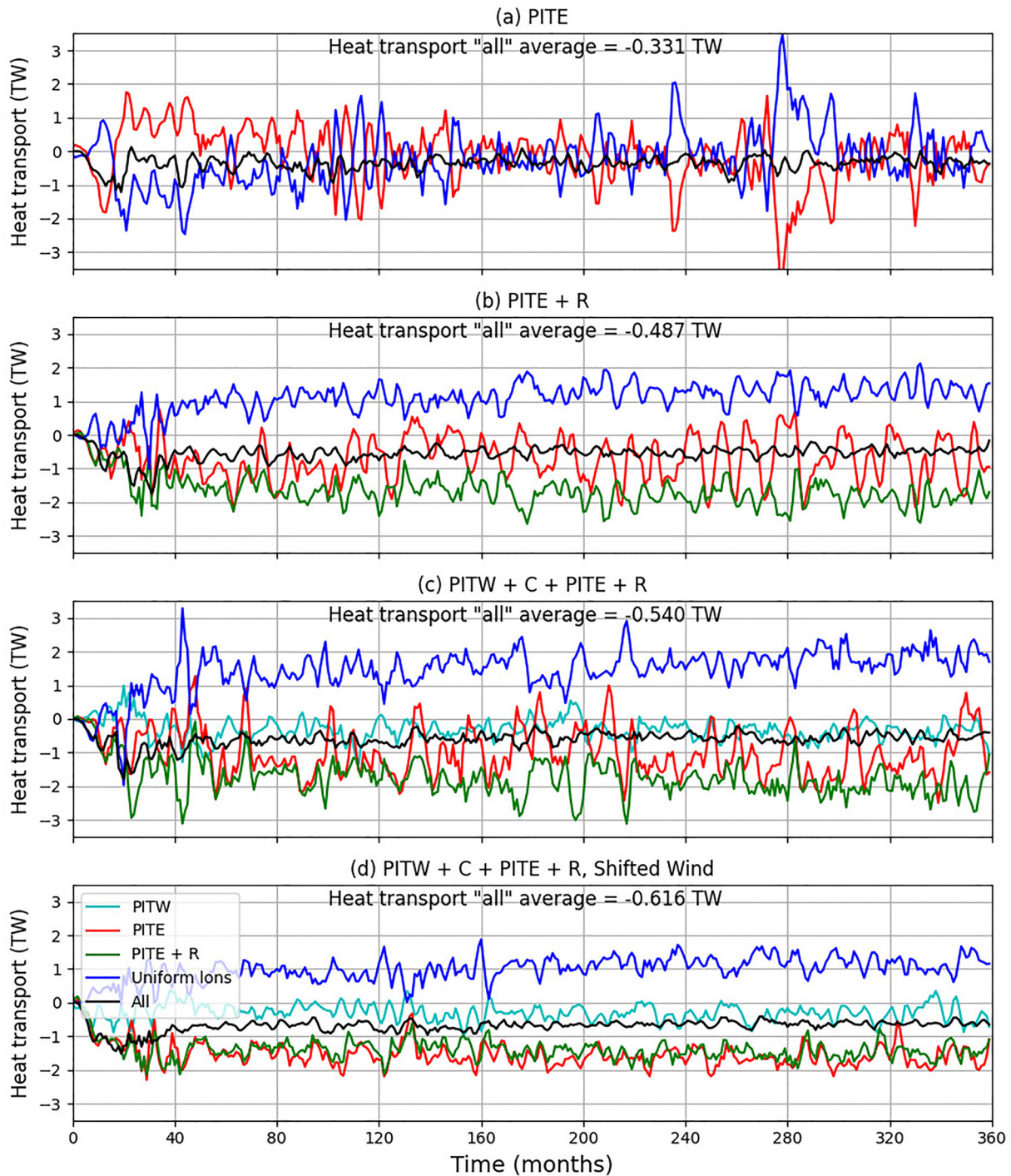
Figure 10. Time series of meridional heat fluxes (units TW) across the shelf break integrated over different longitudinal sections. Negative values denote a heat flux onto the shelf. Results are for simulations with bathymetries with: (a) Pine Island-Thwaites East (PITE) trough only; (b) PITE trough and ridge; (c) both troughs, central basin and ridge. Panel (d) is the same as for panel (c) but with the wind profile shifted southwards by 40 km. We present the heat flux across all longitudes (black), across just the uniform longitudes, that is, where there are no troughs or ridge (blue) and across longitudes with a trough or ridge. The total cross-shelf heat transport averaged over the final 10 years of each simulation is provided in each panel. The presented time series use a 3-monthly running average to aid interpretability. The longitudinal ranges outlining Pine Island-Thwaites West (PITW), PITE and R are shown in Figure 11a.
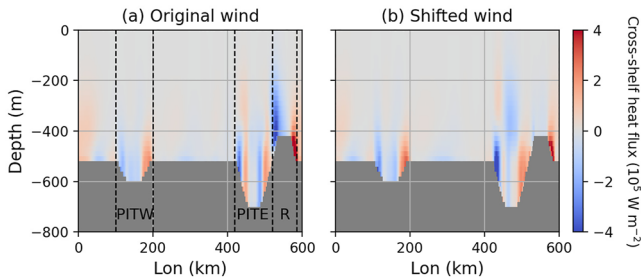
Figure 11. Longitude-depth slices of the cross-shelf break heat flux (through $y = 240$ km), namely $\rho_0 C_p v(\theta - \theta_0)$. These are for simulations with (a) the original wind and (b) the wind shifted southwards 40 km. Both simulations use the idealized bathymetry with the two troughs, the ridge and the central basin. Negative values denote a southward flux. Data area averaged over the final year of 30-year simulations. Dashed lines outline the longitudes over which heat fluxes are integrated for Figure 10.

variability reduces the lengthscales (L) of the local flow regime, increases the Rossby number ($Ro = U/fL$, with velocity scale U) and hence causes the flow to deviate from geostrophic balance (Allen & de Madron, 2009; Allen & Hickey, 2010; Zhang & Lentz, 2018). It is precisely the sharp turns in the along-shelf f/h contours at the trough mouths/ridge (a feature of both regional model and idealized model bathymetries) that reduce the local flow lengthscales. The necessary lengthscale is the radius of curvature (Allen & Hickey, 2010; Klinck & Dinniman, 2010) of the trough mouths/ridge, which is on the order of a few km. We may compare this with the uniform shelf lengthscale of 600 km, suggesting an increase in the Rossby number by two orders of magnitude for flows at the trough mouths. For reference, the local baroclinic deformation radius is $L_d = NH/f$, where N is the buoyancy frequency and H is characteristic depth/scale height. With a density change of 1 kg m^{-3} over a thermocline thickness of 200 m, we estimate $N = 0.0069$ s^{-1} (using $g = 9.81$ m s^{-2} and $\rho_0 = 1{,}030$ kg m^{-3}). Then with $f = -1.4 \times 10^{-4}$ s^{-1} we have $L_d \approx 10$ km.

When the local Rossby number increases, the momentum tendency and momentum advection terms become more important in the meridional momentum budget. This increased role of momentum advection in cross-shelf break exchange is also described by Dinniman and Klinck (2004) and Dinniman et al. (2003). In the vorticity budget, this flow across f/h contours is associated with a balance between vortex stretching and vorticity advection. Figure S5 in Supporting Information S1 illustrates this balance.

With the deviation from geostrophic balance at along-shelf topographic features, the southward pressure gradient force and northward temperature gradient both associated with the ASF induce southward heat fluxes across the shelf break, that is, across f/h contours. Precisely where the fluxes have a tendency to cross the shelf break is different for each topographic configuration and for each trough/ridge. The spatial anomalies in the meridional velocity are small in spatial scale (a few km wide), but since they are excited over topographic variability they have non-zero time mean.

The cases with the ridge have net on-shelf heat fluxes approximately twice as large as the cases without the ridge. In simulations without the ridge the westward along-shelf break current acts as a transport barrier (Ferrari & Nikurashin, 2010) and suppresses heat fluxes onto the shelf. In contrast, simulations with a ridge instead feature a deep cyclonic circulation on the shelf, which does not act as a transport barrier along the entire length of the shelf break. Another important role of the cyclonic circulation is to transport heat fluxed onto the shelf toward the south.

We now consider a longitude-depth slice of the cross-shelf meridional heat flux for the bathymetry with the two troughs, the ridge and the central basin, as shown in Figure 11a. When the eastward undercurrent reaches either trough it turns into the trough on its western side and flows out of the trough on its eastern side. An additional heat flux dipole in the center of the PITE trough is due to a small-scale cyclonic circulation at the trough mouth. In their models with realistic bathymetry, Assmann et al. (2013), Dotto et al. (2020) and Kimura et al. (2017) diagnosed strongest southward heat fluxes across the shelf break at the eastern sides of the troughs, as opposed to the western sides as in our idealized model. This difference is due to inertial overshoots of the eastward undercurrent as it reaches each trough being relatively weak in the idealized model. We note the relatively strong heat fluxes either side of ridge, caused by some of the westward outflow from the bay region passing to the north of the ridge. In doing this, this flow moves northwards upstream of the ridge, crossing f/h contours, before returning southwards downstream of the ridge.

3.3.2. Heat Content

As a measure of the on-shelf heat distribution we use the depth of the $\theta = -0.5°C$ isotherm. We will also use the on-shelf heat content, denoted HC and defined as

$$\text{HC} = \int_\Omega \rho_0 C_p (\theta - \theta_0) \, d\Omega. \tag{1}$$

As before, the reference temperature is $\theta_0 = -1.8°C$. With this choice the only source for on-shelf heat content is from waters fluxed across the shelf break; the initial conditions have an on-shelf heat content of zero. Integration is implemented over the volume Ω, defined to contain the entire zonal range and to span from the southern boundary to the shelf break at $y = 240$ km. Depth integration is applied over the entire water column but
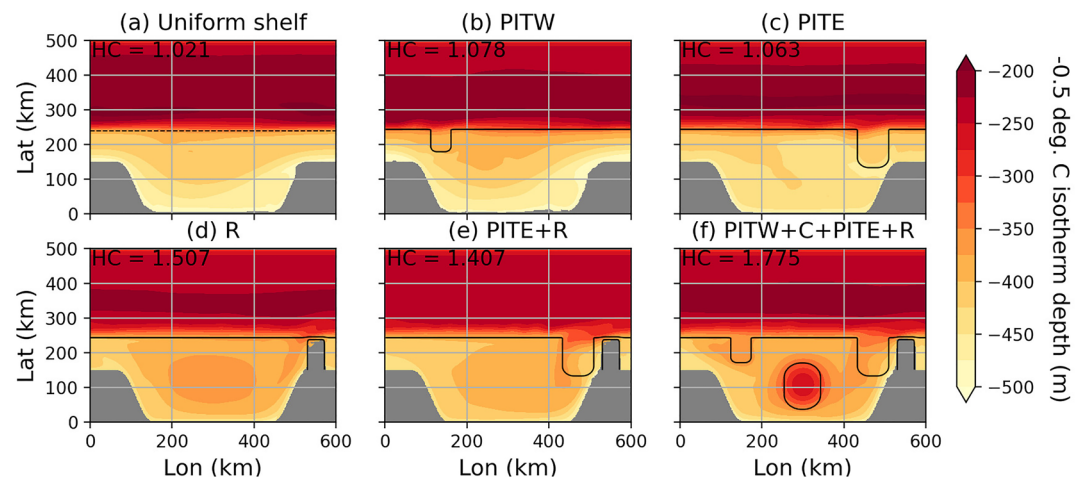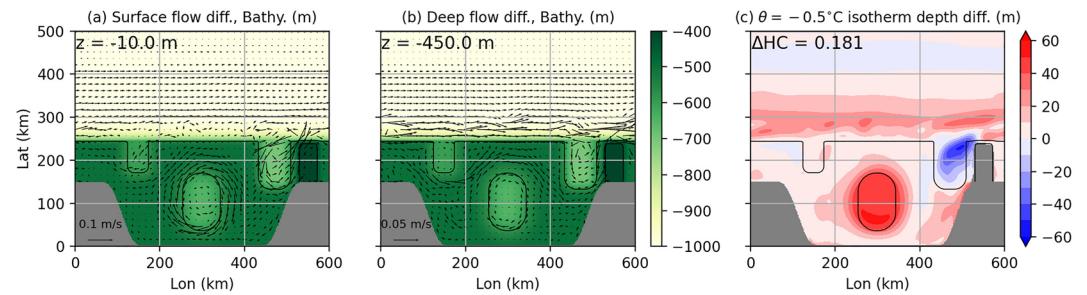
Figure 12. The $\theta = -0.5°C$ isotherm depth for a selection of simulations with different bathymetries. Data is for the isotherm averaged over the final year of the respective 30-year simulations. The six cases are: (a) zonally uniform shelf, (b) shelf with Pine Island-Thwaites West (PITW) trough, (c) shelf with Pine Island-Thwaites East (PITE) trough, (d) shelf with ridge, (e) shelf with PITE trough and ridge, and (f) shelf with PITW, PITE troughs, the central basin and the ridge. Gray masked regions are where the $\theta = -0.5°C$ isotherm does not exist. In each panel we also provide the on-shelf heat content, denoted HC, which is given in units 10^{20} J. The northern boundary of the shelf region is set at a latitude of 240 km, as depicted by the dashed line in (a). In each panel the black contours represent the -580 and -420 m isobaths.

the PITW and PITE troughs at depths greater 500 m are omitted (the central basin is not omitted). We do not consider warm waters within the depths of the troughs as being on the shelf as these waters require an additional upwelling mechanism before they may reach the upper, flat section of the shelf. Furthermore, these warm waters can be contained within large-scale geostrophic currents that flow out of the depths of the troughs shortly after flowing in.

The $\theta = -0.5°C$ isotherm depth is shown in Figure 12 for a selection of bathymetries. Also provided in each panel is the on-shelf heat content (HC). The case of the uniform continental slope (Figure 12a) has the lowest on-shelf heat content (1.021×10^{20} J) due to a relatively stable ASF. The simulations with the PITW (Figure 12b) and PITE (Figure 12c) troughs have marginally greater on-shelf heat contents of 1.078×10^{20} J and 1.063×10^{20} J, respectively. Although in these simulations the troughs can induce cross-shelf exchange of heat, the on-shelf heat content is only marginally greater than in the zonally uniform case because of the along-shelf break flow that acts as a transport barrier (Ferrari & Nikurashin, 2010), inhibiting fluxes of heat onto the shelf.

The simulations with the ridge (Figures 12d–12f) have greater on-shelf heat contents compared to the simulations without a ridge (Figures 12a–12c). The heat content values are 1.507×10^{20} J for the case with just the ridge (Figure 12d), 1.407×10^{20} J for the case with the PITE trough and ridge (Figure 12e), and 1.775×10^{20} J for the case with all topographic features we consider (Figure 12f). These greater heat contents are due to simulations with a ridge featuring a deep cyclonic circulation instead of a strong along-shelf break flow. Unlike the along-shelf break current, the deep cyclonic circulation does not act as a transport barrier along the length of the shelf break.

The deep cyclonic circulation entrains heat fluxed across the shelf break and transports it southwards. The southward transport in the cyclonic circulation is evidenced by the warm tongue in the eastern side of the bay, a feature which also exists in the regional model (Figure 4a). Much of the heat fluxed onto the shelf is stored in a heat "dome" in the center of the shelf. This heat dome is most pronounced and stores the most heat in the simulation with the central basin (Figure 12f). This is the case because the bathymetry gradient around the edges of the central basin permits a steeper stable lateral isotherm gradient because of its suppression of baroclinic instability. That more of the heat fluxed onto the continental shelf is stored in the heat dome means less heat is removed at the southern boundary by the relaxation. A similar heat dome over the deepest part of the central basin is diagnosed in the regional model (Figure 4a) and in the model results of Webber et al. (2019). Dutrieux et al. (2014) and Heywood et al. (2016) have also observed a heat dome in front on Pine Island Glacier.

Figure 13. The flow in the simulation with meridionally shifted winds minus the flow from the simulation with the original winds. We plot results (a) near the surface ($z = -10$ m) and (b) at depth ($z = -450$ m). (c) The difference in the $\theta = -0.5$°C isotherm depth for the same two simulations. Positive values correspond a shallower isotherm, that is, more heat, for the case of shifted winds. For all panels, data are averaged over the last year of 30-year simulations. Black contours represent the -580 and -420 m isobaths.

3.4. A Simulation With Meridionally Shifted Winds

So far in this study we have considered a single wind profile. It is known, though, that the winds in the Amundsen Sea region are highly variable and are changing on climatic timescales (Holland et al., 2022). In recent decades the Southern Hemisphere westerly winds have strengthened and shifted poleward, which is an expected response of the Southern Hemisphere climate to anthropogenic forcings (Arblaster & Meehl, 2006; Gillett et al., 2013; Goyal et al., 2021). Studies have simulated the response to such a wind trend in the Amundsen Sea region (Donat-Magnin et al., 2017) and around the entirety of Antarctica (Spence et al., 2014) in realistic climate simulations and have found that the responses to possible future wind scenarios are complex. However, a consistent prediction is that under these wind changes deep coastal waters are warmed, in turn leading to increased basal melting of the ice shelves.

Motivated by past studies and the recent wind trends, we will use a wind profile obtained by translating the original profile south by 40 km (Figure 5a, dotted curve). This represents a great simplification of actual predicted changes to the winds. For example, in the new profile the winds on the continental shelf are changed, but recent work (Holland et al., 2022) suggests that only winds over the deep ocean have changed and will change due to anthropogenic effects. Given the great simplification in our choice of second wind profile, this section will only be a preliminary investigation into the effects of future wind changes. However, the aim is that this will serve to motivate and inform more comprehensive future investigations.

Figure 13 shows the difference between the flow responses in the simulations with the shifted wind profile and the original wind profile, for the surface layer (Figure 13a, $z = -10$ m) and at depth (Figure 13b, $z = -450$ m). We use the bathymetry with all features of interest; the output a simulation with no bathymetric features is shown in Figure S6 in Supporting Information S1. Shifting the winds southward leads to a weaker westward inflow and marginally stronger on-shelf cyclonic circulation at the surface. A similar acceleration of the cyclonic circulation occurs at depth, with the eastward-flowing section being affected most. This eastward barotropic acceleration as a result of southward shifts in the wind profile over the Amundsen Sea shelf break is a well-known mechanism (Bett et al., 2020; Dotto et al., 2020; Holland et al., 2019; Kimura et al., 2017; Thoma et al., 2008).

In Figure 13c we show the difference between the $\theta = -0.5$°C isotherm depths in the shifted-wind and original-wind simulations. Positive values denote a shallower isotherm (i.e., more heat on shelf) in the simulation with shifted winds. The on-shelf heat content averaged over the final year of the simulation is 1.956×10^{20} J, greater than the heat content of 1.775×10^{20} J in the case of the original winds. The majority of this additional heat in the case of shifted winds is contained within the lateral confines of the central basin.

Figure 10d shows time series of the cross-shelf heat fluxes for the case of southward shifted winds, which can be compared with Figure 10c which is for the original winds. Aggregated over all longitudes, the southward cross-shelf heat flux is marginally greater after shifting the winds, consistent with heat content values. The greater net cross-shelf heat flux and on-shelf heat content is a consequence of weaker off-shelf fluxes at uniform longitudes, this in turn likely due to weaker coastal downwelling in the south. The temporal variability of the heat

fluxes is notably reduced in the case of the shifted winds because the variability of the currents flowing near the shelf break has reduced.

Figure 11b shows a longitude-depth slice of the cross-shelf meridional heat flux for this case with the shifted wind. These cross-shelf break heat fluxes are very similar to those in the case of the original wind profile. The main differences are: (a) a slight strengthening of the shoreward heat flux at the western sides of the troughs, (b) a weakening of the cyclonic circulation and associated heat fluxes in the center of the PITE trough, and (c) a significant weakening of the heat fluxes either side of the ridge.

Our main conclusion here is that a southward shift of the wind profile, which includes an eastward acceleration of the winds at the shelf break, leads to a greater amount of heat on the continental shelf. The wind changes that we have considered here are much simpler than the real-world wind changes which are extremely complex, with natural and anthropogenic trends having different spatial and seasonal patterns. A whole study will be required to conduct a full examination of wind sensitivities.

4. Discussion and Conclusions

In this study we developed a sequence of idealized models of the eastern Amundsen Sea that successfully reproduce the shelf-wide flow as simulated by a regional model. By using idealized models we can make clear conclusions about the roles of winds and bathymetry in shaping the circulation in the region, thus enabling more confident predictions of future changes. We concluded that the deep eastward current on the continental shelf exists because of sufficient blocking of deep inflow from the east by a seabed ridge. The idealized model results also suggest that without the deep current and the associated cyclonic circulation, the shelf would be much cooler. This is because the circulation is favorable for cross-shelf heat fluxes, can entrain heat fluxed across the shelf break, and can transport heat southwards. With no blocking of the deep inflow from the east, a different deep flow would exist, one which enters the eastern Amundsen Sea from the east and exits in the west. This current would remain close to the shelf break and inhibit cross-shelf fluxes by acting as a transport barrier (Ferrari & Nikurashin, 2010).

The idealized model includes weak relaxation of θ and S toward a cold and fresh state at the southern boundary. We repeated these simulations without this southern relaxation (Figure S1 in Supporting Information S1) and find that in steady state the continental shelf is warmer than is realistic, while the flow fields are qualitatively similar to the case with the southern relaxation. That a realistic heat distribution is not attained in the model equilibrium without the southern relaxation highlights the important role that ice-shelf melt plays in maintaining the quasi-mean on-shelf heat content in the regional model and real world.

Many important physical processes are omitted from the idealized model, the inclusion of which could affect the flow responses and heat transport. Mathiot et al. (2017) showed that the introduction of meltwater at depth spins up a cyclonic circulation, suggesting that modeling ice shelf melt in a more realistic manner in the idealized model may lead to a faster cyclonic circulation and greater cross-shelf break heat fluxes. For example, Bett et al. (2020) showed that both ice shelf melt and sea ice melt/formation provide θ and S sources/sinks that are important for maintaining the on-shelf heat distribution in the Amundsen Sea. By not including sea ice in the idealized model, we omit the sea ice-induced convection on the continental shelf. Further, sea ice is known to play an important role in mediating the wind stresses at the ocean's surface (Holland et al., 2019; Zheng et al., 2022). Temporal variability in both the sea ice and surface winds induces seasonal and interannual variability into the regional model and real world. These sources for variability are not included in the idealized model which is forced by a steady surface stress. In addition, the nonlinearity of the dynamics means that steady surface stresses can lead to different flow patterns and cross-shelf fluxes than variable surface stresses that oscillate about the steady profile.

The bathymetry used in the idealized model is a highly simplified representation of that used in the regional model, leading to inevitable differences between the two models' outputs. In particular, the undercurrent's interaction with the troughs is not the same between regional and idealized models. The regional model's output features a strong mean undercurrent that travels along the continental shelf break, onto the continental shelf via the PITW trough and then toward the PITE trough via f/h contours that connect the two troughs. These contours are not represented in the idealized bathymetry, meaning this path for geostrophic flow from the shelf break to the PITE trough via the PITW trough is not included. Nonetheless, our results show why the eastward undercurrent in the Amundsen can turn onto and flow along the northern section of the continental shelf. The regional model

bathymetry is flat nowhere on the shelf, which aids the existence of lateral gradients in density, contributing to baroclinicity in the flow. In contrast, since the idealized model bathymetry is flat away from the defined bathymetric features, the flow is more barotropic than in the regional model. This leads to greater depth-integrated transport in the idealized model relative to the regional model.

The bathymetry in the real world and regional model guides the warm undercurrent toward Pine Island and Thwaites ice shelves. Processes not included in the idealized model are still required for this heat to reach the undersides of the ice shelves; for example, transfer across a ridge at the entrance to Pine Island ice shelf (Bradley et al., 2022; Rydt et al., 2014). In agreement with the regional model, the idealized model shows that much heat fluxed onto the shelf is stored in a heat dome over the deepest on-shelf topography. This feature is also simulated by the regional model and the model of Webber et al. (2019). The storage of heat in the dome leads to a possible lagged effect, whereby heat fluxed onto the shelf is entrained into the heat dome, and is released toward the ice shelves at a later time.

The results of this study mean we now have a clearer insight into why the flow in the Amundsen Sea exists as it does. However, while the focus of this study has been on the role of bottom bathymetry, there is still great uncertainty regarding the true real-world bathymetry in the region. In particular the area between the Amundsen and Bellingshausen Seas on the continental shelf is sparsely mapped (Morlighem, 2020), meaning there is uncertainty regarding the true properties of the ridge. For this reason, future campaigns to map and observe flow in this area would provide invaluable information. Lastly, given the focus on bathymetry in this study, a natural progression is deeper consideration of the buoyancy budget and the role of wind variability in the Amundsen Sea.

Data Availability Statement

The data and post-processing codes used in this study are publicly available for download from Haigh (2023). The data for Figure 2 is available from Dorschel et al. (2022a).

References

Allen, S. E., & de Madron, X. D. (2009). A review of the role of submarine canyons in deep-ocean exchange with the shelf. *Ocean Science*, *5*(4), 607–620. https://doi.org/10.5194/os-5-607-2009

Allen, S. E., & Hickey, B. M. (2010). Dynamics of advection-driven upwelling over a shelf break submarine canyon. *Journal of Geophysical Research*, *115*(C8), C08018. https://doi.org/10.1029/2009jc005731

Arblaster, J. M., & Meehl, G. A. (2006). Contributions of external forcings to southern annular mode trends. *Journal of Climate*, *19*(12), 2896–2905. https://doi.org/10.1175/jcli3774.1

Arneborg, L., Wåhlin, A. K., Björk, G., Liljebladh, B., & Orsi, A. H. (2012). Persistent inflow of warm water onto the central Amundsen shelf. *Nature Geoscience*, *5*(12), 876–880. https://doi.org/10.1038/ngeo1644

Assmann, K. M., Jenkins, A., Shoosmith, D. R., Walker, D. P., Jacobs, S. S., & Nicholls, K. W. (2013). Variability of Circumpolar Deep Water transport onto the Amundsen Sea Continental shelf through a shelf break trough. *Journal of Geophysical Research: Oceans*, *118*(12), 6603–6620. https://doi.org/10.1002/2013jc008871

Bett, D. T., Holland, P. R., Garabato, A. C. N., Jenkins, A., Dutrieux, P., Kimura, S., & Fleming, A. (2020). The impact of the Amundsen Sea freshwater balance on ocean melting of the West Antarctic ice sheet. *Journal of Geophysical Research: Oceans*, *125*(9), e2020JC016305. https://doi.org/10.1029/2020jc016305

Bradley, A. T., Bett, D. T., Dutrieux, P., Rydt, J. D., & Holland, P. R. (2022). The influence of pine Island Ice Shelf calving on basal melting. *Journal of Geophysical Research: Oceans*, *127*(9), e2022JC018621. https://doi.org/10.1029/2022jc018621

Caillet, J., Jourdain, N. C., Mathiot, P., Hellmer, H. H., & Mouginot, J. (2022). Drivers and reversibility of abrupt ocean state transitions in the Amundsen Sea, Antarctica. *Journal of Geophysical Research: Oceans*, *128*(1), e2022JC018929. https://doi.org/10.1029/2022jc018929

Chavanne, C. P., Heywood, K. J., Nicholls, K. W., & Fer, I. (2010). Observations of the Antarctic slope undercurrent in the southeastern Weddell Sea. *Geophysical Research Letters*, *37*(13), n/a. https://doi.org/10.1029/2010gl043603

Chen, C., & Kamenkovich, I. (2013). Effects of topography on baroclinic instability. *Journal of Physical Oceanography*, *43*(4), 790–804. https://doi.org/10.1175/jpo-d-12-0145.1

Chen, S.-N., Chen, C.-J., & Lerczak, J. A. (2020). On baroclinic instability over continental shelves: Testing the utility of Eady-type models. *Journal of Physical Oceanography*, *50*(1), 3–33. https://doi.org/10.1175/jpo-d-19-0175.1

Dinniman, M. S., & Klinck, J. M. (2004). A model study of circulation and cross-shelf exchange on the west Antarctic Peninsula continental shelf. *Deep Sea Research Part II: Topical Studies in Oceanography*, *51*(17–19), 2003–2022. https://doi.org/10.1016/j.dsr2.2004.07.030

Dinniman, M. S., Klinck, J. M., & Smith, W. O. (2003). Cross-shelf exchange in a model of the Ross Sea circulation and biogeochemistry. *Deep Sea Research Part II: Topical Studies in Oceanography*, *50*(22–26), 3103–3120. https://doi.org/10.1016/j.dsr2.2003.07.011

Donat-Magnin, M., Jourdain, N. C., Spence, P., Sommer, J. L., Gallée, H., & Durand, G. (2017). Ice-shelf melt response to changing winds and glacier dynamics in the Amundsen Sea Sector, Antarctica. *Journal of Geophysical Research: Oceans*, *122*(12), 10206–10224. https://doi.org/10.1002/2017jc013059

Dong, J., Speer, K., & Jullion, L. (2016). The Antarctic Slope Current near 30°E. *Journal of Geophysical Research: Oceans*, *121*(2), 1051–1062. https://doi.org/10.1002/2015jc011099

Dorschel, B., Hehemann, L., Viquerat, S., Warnke, F., Dreutter, S., Tenberge, Y. S., et al. (2022a). The international bathymetric chart of the Southern Ocean version 2 (IBCSO v2) [Dataset]. PANGAEA. https://doi.org/10.1594/PANGAEA.937574

Dorschel, B., Hehemann, L., Viquerat, S., Warnke, F., Dreutter, S., Tenberge, Y. S., et al. (2022b). The international bathymetric chart of the Southern Ocean version 2. *Scientific Data*, *9*(1), 275. https://doi.org/10.1038/s41597-022-01366-7

Dotto, T. S., Garabato, A. C. N., Bacon, S., Holland, P. R., Kimura, S., Firing, Y. L., et al. (2019). Wind-driven processes controlling oceanic heat delivery to the Amundsen Sea, Antarctica. *Journal of Physical Oceanography*, *49*(11), 2829–2849. https://doi.org/10.1175/jpo-d-19-0064.1

Dotto, T. S., Garabato, A. C. N., Wåhlin, A. K., Bacon, S., Holland, P. R., Kimura, S., et al. (2020). Control of the oceanic heat content of the Getz-Dotson trough, Antarctica, by the Amundsen Sea low. *Journal of Geophysical Research: Oceans*, *125*(8), e2020JC016113. https://doi.org/10.1029/2020jc016113

Dutrieux, P., Rydt, J. D., Jenkins, A., Holland, P. R., Ha, H. K., Lee, S. H., et al. (2014). Strong sensitivity of Pine Island ice-shelf melting to climatic variability. *Science*, *343*(6167), 174–178. https://doi.org/10.1126/science.1244341

Favier, L., Durand, G., Cornford, S. L., Gudmundsson, G. H., Gagliardini, O., Gillet-Chaulet, F., et al. (2014). Retreat of Pine Island Glacier controlled by marine ice-sheet instability. *Nature Climate Change*, *4*(2), 117–121. https://doi.org/10.1038/nclimate2094

Ferrari, R., & Nikurashin, M. (2010). Suppression of eddy diffusivity across jets in the Southern Ocean. *Journal of Physical Oceanography*, *40*(7), 1501–1519. https://doi.org/10.1175/2010jpo4278.1

Gillett, N. P., Fyfe, J. C., & Parker, D. E. (2013). Attribution of observed sea level pressure trends to greenhouse gas, aerosol, and ozone changes. *Geophysical Research Letters*, *40*(10), 2302–2306. https://doi.org/10.1002/grl.50500

Goyal, R., Gupta, A. S., Jucker, M., & England, M. H. (2021). Historical and projected changes in the southern hemisphere surface westerlies. *Geophysical Research Letters*, *48*(4), e2020GL090849. https://doi.org/10.1029/2020gl090849

Haigh, M. (2023). Data for the influence of bathymetry over heat transport onto the Amundsen Sea continental shelf [Dataset]. Zenodo. https://doi.org/10.5281/ZENODO.7695558

Heywood, K., Biddle, L., Boehme, L., Dutrieux, P., Fedak, M., Jenkins, A., et al. (2016). Between the devil and the deep blue sea: The role of the Amundsen Sea Continental Shelf in exchanges between ocean and ice shelves. *Oceanography*, *29*(4), 118–129. https://doi.org/10.5670/oceanog.2016.104

Holland, P. R., Bracegirdle, T. J., Dutrieux, P., Jenkins, A., & Steig, E. J. (2019). West Antarctic ice loss influenced by internal climate variability and anthropogenic forcing. *Nature Geoscience*, *12*(9), 718–724. https://doi.org/10.1038/s41561-019-0420-9

Holland, P. R., O'Connor, G. K., Bracegirdle, T. J., Dutrieux, P., Naughten, K. A., Steig, E. J., et al. (2022). Anthropogenic and internal drivers of wind changes over the Amundsen Sea, West Antarctica, during the 20th and 21st centuries. *The Cryosphere*, *16*(12), 5085–5105. https://doi.org/10.5194/tc-16-5085-2022

Jacobs, S. S. (1991). On the nature and significance of the Antarctic Slope Front. *Marine Chemistry*, *35*(1–4), 9–24. https://doi.org/10.1016/s0304-4203(09)90005-6

Jacobs, S. S., Hellmer, H. H., & Jenkins, A. (1996). Antarctic ice sheet melting in the southeast Pacific. *Geophysical Research Letters*, *23*(9), 957–960. https://doi.org/10.1029/96gl00723

Jacobs, S. S., Jenkins, A., Hellmer, H., Giulivi, C., Nitsche, F., Huber, B., & Guerrero, R. (2012). The Amundsen Sea and the Antarctic ice sheet. *Oceanography*, *25*(3), 154–163. https://doi.org/10.5670/oceanog.2012.90

Jenkins, A., Dutrieux, P., Jacobs, S., Steig, E., Gudmundsson, H., Smith, J., & Heywood, K. (2016). Decadal ocean forcing and Antarctic ice sheet response: Lessons from the Amundsen Sea. *Oceanography*, *29*(4), 106–117. https://doi.org/10.5670/oceanog.2016.103

Jenkins, A., Shoosmith, D., Dutrieux, P., Jacobs, S., Kim, T. W., Lee, S. H., et al. (2018). West Antarctic ice sheet retreat in the Amundsen Sea driven by decadal oceanic variability. *Nature Geoscience*, *11*(10), 733–738. https://doi.org/10.1038/s41561-018-0207-4

Joughin, I., Smith, B. E., & Medley, B. (2014). Marine ice sheet collapse potentially under way for the Thwaites Glacier Basin, West Antarctica. *Science*, *344*(6185), 735–738. https://doi.org/10.1126/science.1249055

Jourdain, N. C., Mathiot, P., Burgard, C., Caillet, J., & Kittel, C. (2022). Ice shelf basal melt rates in the Amundsen Sea at the end of the 21st century. *Geophysical Research Letters*, *49*(22), e2022GL100629. https://doi.org/10.1029/2022gl100629

Jourdain, N. C., Mathiot, P., Merino, N., Durand, G., Sommer, J. L., Spence, P., et al. (2017). Ocean circulation and sea-ice thinning induced by melting ice shelves in the Amundsen Sea. *Journal of Geophysical Research: Oceans*, *122*(3), 2550–2573. https://doi.org/10.1002/2016jc012509

Jourdain, N. C., Molines, J.-M., Sommer, J. L., Mathiot, P., Chanut, J., de Lavergne, C., & Madec, G. (2019). Simulating or prescribing the influence of tides on the Amundsen Sea ice shelves. *Ocean Modelling*, *133*, 44–55. https://doi.org/10.1016/j.ocemod.2018.11.001

Kimura, S., Jenkins, A., Regan, H., Holland, P. R., Assmann, K. M., Whitt, D. B., et al. (2017). Oceanographic controls on the variability of ice-shelf basal melting and circulation of glacial meltwater in the Amundsen Sea Embayment, Antarctica. *Journal of Geophysical Research: Oceans*, *122*(12), 10131–10155. https://doi.org/10.1002/2017jc012926

Klinck, J. M., & Dinniman, M. S. (2010). Exchange across the shelf break at high southern latitudes. *Ocean Science*, *6*(2), 513–524. https://doi.org/10.5194/os-6-513-2010

Large, W. G., McWilliams, J. C., & Doney, S. C. (1994). Oceanic vertical mixing: A review and a model with a nonlocal boundary layer parameterization. *Reviews of Geophysics*, *32*(4), 363. https://doi.org/10.1029/94rg01872

Mathiot, P., Jenkins, A., Harris, C., & Madec, G. (2017). Explicit representation and parametrised impacts of under ice shelf seas in the *z** coordinate ocean model NEMO 3.6. *Geoscientific Model Development*, *10*(7), 2849–2874. https://doi.org/10.5194/gmd-10-2849-2017

Mazloff, M. R., Heimbach, P., & Wunsch, C. (2010). An eddy-permitting Southern Ocean state estimate. *Journal of Physical Oceanography*, *40*(5), 880–899. https://doi.org/10.1175/2009jpo4236.1

Moffat, C., Beardsley, R. C., Owens, B., & van Lipzig, N. (2008). A first description of the Antarctic Peninsula Coastal Current. *Deep Sea Research Part II: Topical Studies in Oceanography*, *55*(3–4), 277–293. https://doi.org/10.1016/j.dsr2.2007.10.003

Morlighem, M. (2020). *MEaSUREs BedMachine Antarctica, version 2*. NASA National Snow and Ice Data Center Distributed Active Archive Center. https://doi.org/10.5067/E1QL9HFQ7A8M

Mouginot, J., Rignot, E., & Scheuchl, B. (2014). Sustained increase in ice discharge from the Amundsen Sea Embayment, West Antarctica, from 1973 to 2013. *Geophysical Research Letters*, *41*(5), 1576–1584. https://doi.org/10.1002/2013gl059069

Nakayama, Y., Menemenlis, D., Zhang, H., Schodlok, M., & Rignot, E. (2018). Origin of Circumpolar Deep Water intruding onto the Amundsen and Bellingshausen Sea continental shelves. *Nature Communications*, *9*(1), 3403. https://doi.org/10.1038/s41467-018-05813-1

Naughten, K. A., Holland, P. R., Dutrieux, P., Kimura, S., Bett, D. T., & Jenkins, A. (2022). Simulated twentieth-century ocean warming in the Amundsen Sea, West Antarctica. *Geophysical Research Letters*, *49*(5), e2021GL094566. https://doi.org/10.1029/2021gl094566

Ou, H.-W. (2007). Watermass properties of the Antarctic Slope Front: A simple model. *Journal of Physical Oceanography*, *37*(1), 50–59. https://doi.org/10.1175/jpo2981.1

Petty, A. A., Feltham, D. L., & Holland, P. R. (2013). Impact of atmospheric forcing on Antarctic Continental shelf water masses. *Journal of Physical Oceanography*, *43*(5), 920–940. https://doi.org/10.1175/jpo-d-12-0172.1

Pritchard, H. D., Ligtenberg, S. R. M., Fricker, H. A., Vaughan, D. G., van den Broeke, M. R., & Padman, L. (2012). Antarctic ice-sheet loss driven by basal melting of ice shelves. *Nature*, *484*(7395), 502–505. https://doi.org/10.1038/nature10968

Raphael, M. N., Marshall, G. J., Turner, J., Fogt, R. L., Schneider, D., Dixon, D. A., et al. (2016). The Amundsen Sea low: Variability, change, and impact on Antarctic climate. *Bulletin of the American Meteorological Society*, *97*(1), 111–121. https://doi.org/10.1175/bams-d-14-00018.1

Rignot, E., Bamber, J. L., van den Broeke, M. R., Davis, C., Li, Y., van de Berg, W. J., & van Meijgaard, E. (2008). Recent Antarctic ice mass loss from radar interferometry and regional climate modelling. *Nature Geoscience*, *1*(2), 106–110. https://doi.org/10.1038/ngeo102

Rignot, E., Mouginot, J., Morlighem, M., Seroussi, H., & Scheuchl, B. (2014). Widespread, rapid grounding line retreat of Pine Island, Thwaites, Smith, and Kohler glaciers, West Antarctica, from 1992 to 2011. *Geophysical Research Letters*, *41*(10), 3502–3509. https://doi.org/10.1002/2014gl060140

Rydt, J. D., Holland, P. R., Dutrieux, P., & Jenkins, A. (2014). Geometric and oceanographic controls on melting beneath Pine Island Glacier. *Journal of Geophysical Research: Oceans*, *119*(4), 2420–2438. https://doi.org/10.1002/2013jc009513

Schubert, R., Thompson, A. F., Speer, K., Chretien, L. S., & Bebieva, Y. (2021). The Antarctic Coastal Current in the Bellingshausen Sea. *The Cryosphere*, *15*(9), 4179–4199. https://doi.org/10.5194/tc-15-4179-2021

Shepherd, A., Ivins, E., Rignot, E., Smith, B., van den Broeke, M., Velicogna, I., et al. (2018). Mass balance of the Antarctic ice sheet from 1992 to 2017. *Nature*, *558*(7709), 219–222. https://doi.org/10.1038/s41586-018-0179-y

Spence, P., Griffies, S. M., England, M. H., Hogg, A. M., Saenko, O. A., & Jourdain, N. C. (2014). Rapid subsurface warming and circulation changes of Antarctic coastal waters by poleward shifting winds. *Geophysical Research Letters*, *41*(13), 4601–4610. https://doi.org/10.1002/2014gl060613

Stewart, A. L., Klocker, A., & Menemenlis, D. (2019). Acceleration and overturning of the Antarctic Slope Current by winds, eddies, and tides. *Journal of Physical Oceanography*, *49*(8), 2043–2074. https://doi.org/10.1175/jpo-d-18-0221.1

Stewart, A. L., & Thompson, A. F. (2013). Connecting Antarctic cross-slope exchange with Southern Ocean overturning. *Journal of Physical Oceanography*, *43*(7), 1453–1471. https://doi.org/10.1175/jpo-d-12-0205.1

Stewart, A. L., & Thompson, A. F. (2015). Eddy-mediated transport of warm Circumpolar Deep Water across the Antarctic shelf break. *Geophysical Research Letters*, *42*(2), 432–440. https://doi.org/10.1002/2014gl062281

Thoma, M., Jenkins, A., Holland, D., & Jacobs, S. (2008). Modelling Circumpolar Deep Water intrusions on the Amundsen Sea continental shelf, Antarctica. *Geophysical Research Letters*, *35*(18), L18602. https://doi.org/10.1029/2008gl034939

Thompson, A. F., Speer, K. G., & Chretien, L. M. S. (2020). Genesis of the Antarctic Slope Current in West Antarctica. *Geophysical Research Letters*, *47*(16), e2020GL087802. https://doi.org/10.1029/2020gl087802

Thompson, A. F., Stewart, A. L., Spence, P., & Heywood, K. J. (2018). The Antarctic Slope Current in a changing climate. *Reviews of Geophysics*, *56*(4), 741–770. https://doi.org/10.1029/2018rg000624

Vallis, G. (2017). Barotropic and baroclinic instability. In *Atmospheric and oceanic fluid dynamics* (pp. 335–378). Cambridge University Press. https://doi.org/10.1017/9781107588417.010

Walker, D. P., Brandon, M. A., Jenkins, A., Allen, J. T., Dowdeswell, J. A., & Evans, J. (2007). Oceanic heat transport onto the Amundsen Sea shelf through a submarine glacial trough. *Geophysical Research Letters*, *34*(2), L02602. https://doi.org/10.1029/2006gl028154

Walker, D. P., Jenkins, A., Assmann, K. M., Shoosmith, D. R., & Brandon, M. A. (2013). Oceanographic observations at the shelf break of the Amundsen Sea, Antarctica. *Journal of Geophysical Research: Oceans*, *118*(6), 2906–2918. https://doi.org/10.1002/jgrc.20212

Webber, B. G. M., Heywood, K. J., Stevens, D. P., & Assmann, K. M. (2019). The impact of overturning and horizontal circulation in Pine Island trough on ice shelf melt in the Eastern Amundsen Sea. *Journal of Physical Oceanography*, *49*(1), 63–83. https://doi.org/10.1175/jpo-d-17-0213.1

Zhang, W., & Lentz, S. J. (2018). Wind-driven circulation in a shelf valley. Part II: Dynamics of the along-valley velocity and transport. *Journal of Physical Oceanography*, *48*(4), 883–904. https://doi.org/10.1175/jpo-d-17-0084.1

Zheng, Y., Stevens, D. P., Heywood, K. J., Webber, B. G. M., & Queste, B. Y. (2022). Reversal of ocean gyres near ice shelves in the Amundsen Sea caused by the interaction of sea ice and wind. *The Cryosphere*, *16*(7), 3005–3019. https://doi.org/10.5194/tc-16-3005-2022